Taking it to the next level: Searching for gravitational waves with eccentricity from compact binary coalescences

Author: Elwin K. Y. Li[1],
Mentor: Alan J. Weinstein[2]
Hong Kong University of Science and Technology, Clear Water Bay, Kowloon, Hong Kong[1]
LIGO Laboratory, California Institute of Technology, Pasadena, CA 91125, USA[2]
Email: kyeliaa@connect.ust.hk[1], ajw@caltech.edu[2]
(Dated: August 8, 2023)

Gravitational waves (GWs)[1, 2] are fundamental predictions of the General Theory of Relativity (GR). GWs detections have introduced a novel window into the universe and are revolutionizing our understanding of astrophysics. The motion of two massive objects in an eccentric orbit emits GWs which carry information about the eccentricity of the binary black hole (BBH) source. These waveforms are characterized by their eccentricity, which measures the deviation of the orbit from a quasi-circular orbit. Studying eccentric binary orbits provides evidence for the dynamic formation of the binary system. In this project, we study a new family of GWs waveforms from eccentric binaries and their implications for detecting and analyzing eccentric compact binary systems near mergers. I will develop eccentric waveform models and parameter estimation frameworks for eccentric BBH and use these tools to analyze the data from current and upcoming GWs observations. Since eccentric waveforms are predicted to have similar waveforms with GWs from BBH systems with precessing, I will try to distinguish eccentric waveforms and precessing waveforms by investigating their differences. We will determine the minimum eccentricity that could be detectable with GWs as a function of SNR and other parameters.

I. INTRODUCTION AND MOTIVATION

A. Background

The discovery of GWs, initially proposed by GR[3–6], has brought a new observational window on the cosmos. Exploring the properties of GWs can provide us with fresh perspectives into the properties of massive compact objects (neutron stars and black holes) in the universe and their role in the evolution of galaxies.

B. Gravitational Waves

GWs are ripples in space-time, which propagate outward at the speed of light, generated by the acceleration of massive objects. BBH mergers and binary neutron star (BNS) mergers are compact binary coalescences (CBCs) that generate detectable gravitational waves. Since the distance of CBCs from Earth is extremely far, GWs generated are extremely weak and hard to detect when they reach the Earth. They were first predicted in 1916 by GR. GWs have a property called polarization, which describes the orientation of the ripples. Just as electromagnetic waves have different polarizations (linear, circular, or elliptical), GWs can also have different polarizations. GWs have two transverse polarization modes: plus-polarization (h_+) and cross-polarization (h_+). The terms plus and the cross will be collectively known as the linear polarization basis. They stretch and compress the space-time in the two directions orthogonal to the direction of propagation[7]. h_+ is like the stretching and squeezing of space-time in GWs with a 45-degree angle. The impact on test particles in a h_x GWs would be similar to that of a regular polarized GWs but with a 45-degree rotation.

C. Gravitational Wave Detectors

Nowadays, gravitational waves can be detected by gravitational waves observatories[8], including Advanced LIGO (aLIGO)[9], VIRGO[10], and Kagra[11], which already have conducted three observing runs[12–14] in total. Figure 1 shows the configuration of the laser interferometer at the heart of the LIGO detectors and the laser mirrors (test masses) on their quadruple-pendulum suspensions. Since the two arms have the same nominal length, the split laser beams will have destructive interference at the output port when joined at the beam splitter, and the detector will register no signal. When GWs pass through the detector, the arms will be stretched or compressed, resulting in length differences. The interference pattern will then be partially constructive such that a weak signal can be detected at the output port.

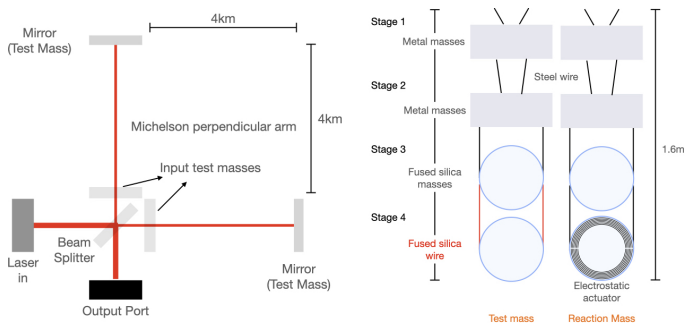

Figure 1. Interferometer configuration (Left) and test mass setup (Right).

D. Eccentric Binaries

When two massive objects move in an eccentric orbit, they generate GWs waveforms that encode the eccentricity - eccentric waveforms. The eccentricity of these waveforms reflects the extent of orbit deviation from a perfect circle. For a quasi-circular orbit (since eccentricity = 0), there are fifteen parameters (sixteen for BNS) to determine GWs, including the masses of the two mergers, the spin of the two mergers in three different directions (x, y, and z directions for both compact objects), source distance, sky location (right ascension and declination), coalescence time, coalescence phase, inclination and polarization (and tidal deformability for BNS), in which eccentricity is not one of the parameters. Since GWs are dominantly quadrupolar radiation, the frequencies of GWs (f_{GW}) are doubled that of the orbital frequencies (f_{orb}). Our detectors cannot detect GWs when f_{GW} is lower than 20Hz. The problem is that the orbit could be eccentric initially but become less eccentric or nearly circular when the two sources are getting close with an orbital frequency higher than 20Hz. If the eccentricity is high at $f_{GW} = 20$Hz, it is predicted to approach zero by the time $f_{orb} = 50$Hz.

BBHs are common in the universe. BBH systems may form through common evolution in isolation (first column of Fig 2). Another possibility is dynamical capture, in which the binary system is formed by capturing other massive objects (second column in Fig. 2). Other formation mechanisms are predicted as well. We do not know which of these formation mechanisms are dominant for systems that merge in the LIGO frequency band.

In GWs astrophysics, it is important to investigate eccentric gravitational waveforms as they can offer valuable information about the formation characteristics of BBH. Several studies[15, 16] have been conducted on eccentric gravitational waveforms based on the standard approach and a novel method suggested[17], which uses parameter estimation. These investigations offer new perspectives into the characteristics of these waveforms and their possible uses in examining the cosmos.

E. BBH Formation in Isolation and Dynamical Capture

One of our primary goals is to understand how compact binary systems form. One possibility is the BBH Formation in Isolation, in which a binary system evolves together, undergoes Roche lobe overflow and a common envelope stage that tightens the binary orbit through dynamical friction. One of the stars will directly turn into a black hole. If a common envelope occurs, the giant envelope will surround the orbit of the system. Thermal energy is transferred to the envelope and may trigger the ejection of the envelope. Once the ejection of the envelope occurs, the massive star will directly turn into a black hole, leading to the inspiral of the two black holes and merging into a single one at the end. This BBH formation and merger is a common evolution in which the orbit is quasi-circular, with eccentricity close to zero. Another possibility is BBH formation in dense star clusters (e.g., at the center of galaxies or in globular clusters) through dynamical capture. The binary massive star system undergoes a similar process as the BBH formation in isolation unless another massive BH is captured by the cross-section area of the two stars, ejecting the massive stars out of the original orbit and forming a new BBH system.[18] Since the new-coming BH removed some orbital energy from the initial orbit, the orbit is highly eccentric. This process is called the dynamical capture. The probability of dynamic capture is related to the capture cross-section. Another scenario of BBH Formation by dynamical capture is when a fast-moving BH is being captured by another BH. Figure 2 shows the evolution of the three BBH formation mechanisms. There are three of the many examples of BBH formation. Other examples also exist and contribute to BBH capture or formation. The study of eccentric GWs provides valuable information to determine which form of BBH system dominates. We also want to look for dynamic capture with a very small cross-section such that the time of the merger is within seconds.

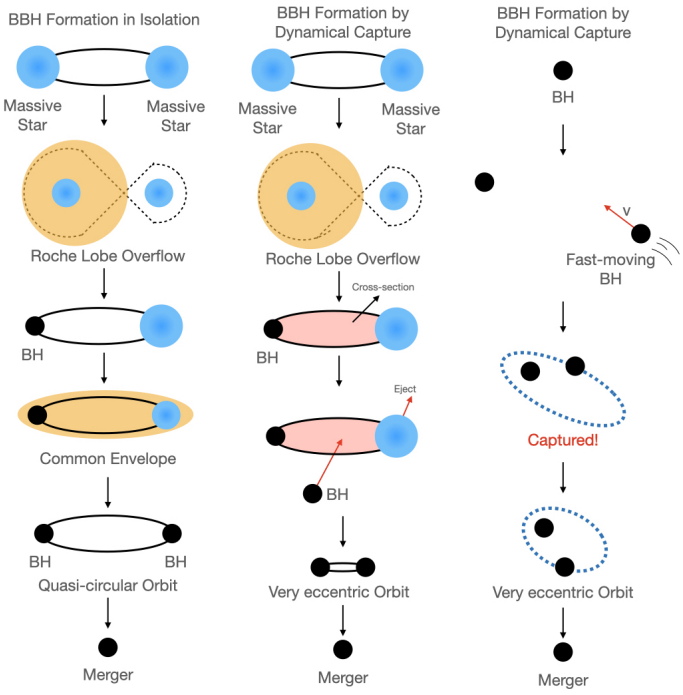

Figure 2. Following Michela Mapelli et al., BBH Formation in Isolation (Left) and by Dynamical Capture (Right)[18]. Another scenario of BBH Formation by Dynamical Capture (Middle).

F. Matched-filtering

Matched-filtering[19], with PyCBC[20–22] search pipeline is a technique that can detect numerous possible GWs candidates from a given period with similar shapes. It can detect signals from stationary Gaussian noise by sliding the template

waveforms across the data and calculating the SNR.

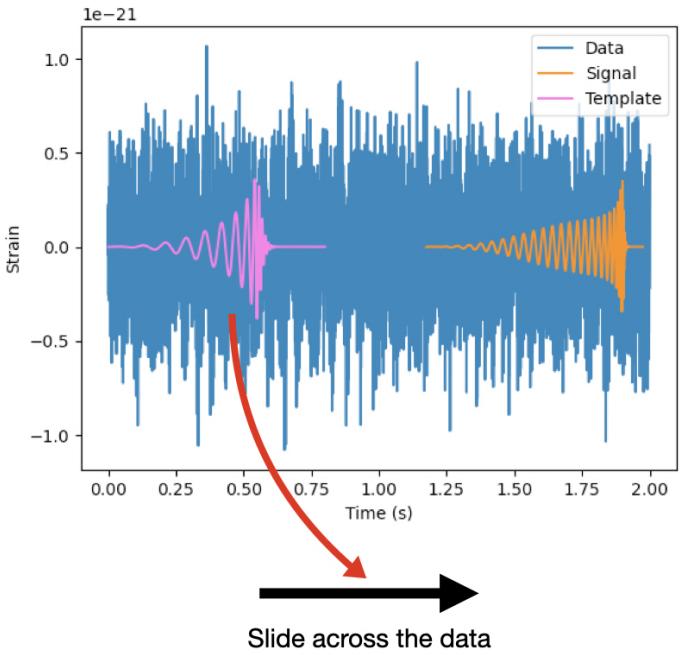

Figure 3. A figure visualizing the process of matched-filtering.

Suppose $n(t)$ is the stationary Gaussian noise process, $S_n(f)$ is the one-sided power spectral density (PSD) given by

$$\langle \tilde{n}(f)\tilde{n}^*(f')\rangle = \frac{1}{2}S_n(|f|)\delta(f-f'), \tag{1}$$

the matched-filtering output of a data stream is

$$x(t_0) = 2\int_{-\infty}^{\infty} \frac{\tilde{s}(f)\tilde{h}^*_{template}(f)}{S_n(f)}df \tag{2}$$

which may only contain noise $s(t) = n(t)$, or signal with noise $s(t) = n(t) + h(t)$ where $h(t)$ is the signal. Denote $h_{template}(t)$ as the filter template. Since there are unknown parameters (amplitude, coalescence phase, and binary com[anion masses) in the waveform, the "best match" unknown phase ϕ_0 has to be found by maximizing $x(t_0)$ over ϕ_0. $x(t_0)$ is defined as

$$x(t_0) = x_{re}(t_0)cos2\phi_0 + x_{im}(t_0)sin2\phi_0, \tag{3}$$

where $x_{re,im}$ can be found by using Eq. 2 with $\phi_0 = 0$. Therefore, the maximum value can be found using the equation

$$x^2(t_0)|_{\hat{\phi_0}maximum} = x^2_{re}(t_0) + x^2_{i,}(t_0) \tag{4}$$

at $2\hat{\phi_0} = arg(x_{re} + ix_{im})$. The modulus of complex filter output then gives the maximum:

$$z(t_0) = x_{re}(t_0) + ix_{im}(t_0) \tag{5}$$

$$= 4\mathbb{R}\int_0^{\infty} \frac{\tilde{s}(f)(\tilde{h}^*_{template}(f))_0}{S_n(f)}e^{2\pi i f t_0}df, \tag{6}$$

where $(\tilde{h}^*_{template}(f))_0 = (\tilde{h}^*_{template}(f))_{t_0=0,\phi_0=0}$. The normalization constant for each template is calculated by

$$\sigma^2_m = 4\int_0^{\infty} \frac{|\tilde{h}_{1Mpc,m}(f)|^2}{S_n(f)}df, \tag{7}$$

such that the Signal-to-Noise Ratio (SNR) can be calculated afterward. The amplitude SNR of the quadrature matched-filtering is given by

$$\rho_m(t) = \frac{|z_m(t)|}{\sigma_m}. \tag{8}$$

If the signal is absent, then

$$< \rho^2_m >= 2. \tag{9}$$

Since for purely static and Gaussian noise, obtaining $\rho_m >> 1$ is improbable, a lower threshold on ρ_m is often used to identify event candidates.

For each trigger, a False-Alarm-Probability (FAP), which is the probability that noise can produce a trigger with a ranking statistic $\ln \mathcal{L} \geq \ln \mathcal{L}^*$, will be calculated as

$$\mathbf{FAP} = P(\ln \mathcal{L} > \ln \mathcal{L}^* | \mathbf{noise}) = \int_{\ln \mathcal{L}^*}^{\infty} P(\ln \mathcal{L}|\mathbf{noise}) d\ln \mathcal{L} \tag{10}$$

The lower the FAP, the more likely the trigger comes from an actual GWs signal.

G. Bilby and Parameter Estimation

Bilby[23], an interface for performing parameter estimation (PE)[24], aims to deduce parameters of CBCs waveforms. It uses the Bilby Markov chain Monte Carlo (BILBY-MCMC)[25] sampling algorithm to map out the possible parameters of the waveforms.

1. *Bayes Formula and Probability Density Function*

Bayes Formula represents a statistical equation to determine the likelihood of a particular event happening under specific conditions. The probability of an event A given a condition B is given by

$$P(A \mid B) = \frac{P(A \cap B)}{P(B)}. \tag{11}$$

The probability of B given A is given by

$$P(B \mid A) = \frac{P(B \cap A)}{P(A)} = \frac{P(A \cap B)}{P(A)}. \tag{12}$$

By substituting Equation 12 into Equation 11, we get

$$P(A \mid B) = \frac{P(B \mid A)P(A)}{P(B)}, \tag{13}$$

which is the Bayes Formula.

The probability Density Function (PDF), or the posterior probability, is the probability of an event given a condition. In GWs PE, it is used to find out the probability that the estimating parameters θ can describe the data d by

$$P(\theta \mid d) = \frac{P(d \mid \theta)P(\theta)}{P(d)}, \tag{14}$$

where $P(d \mid \theta)$ is called the likelihood, $P(\theta)$ is called the prior, $P(d)$ is called the evidence. It is challenging to find the probability that θ can describe d in reality but easy to find the probability that d can describe the data θ. One can calculate $P(\theta \mid d)$ using PDF.

The likelihood is the probability of the condition given the event. In GWs PE, the likelihood $\mathcal{L}(d \mid \theta)$ is the probability of d with the given θ. For each frequency, $\mathcal{L}(d_i \mid \theta)$ is given by

$$\mathcal{L}(d_i \mid \theta) = \frac{2\Delta f}{\pi S_n(f_i)} \exp\left(-2\Delta f \frac{(d(f_i) - h(f_i, \theta))^2}{S_n(f_i)}\right), \tag{15}$$

where $d(f_i)$ is the data, $h(f_i, \theta)$ is the signal, $d(f_i) - h(f_i, \theta)$ is the noise. The total $\mathcal{L}(d \mid \theta)$ is given by

$$\ln\left(\mathcal{L}(d \mid \theta)\right) = \sum_{i=1} \ln \mathcal{L}(d_i \mid \theta), \tag{16}$$

The prior is the probability of the event without any information. In GWs PE, it can be seen as the "degree of believe" that θ is true.

The evidence is the probability of the condition without any information. It usually uses to compare the event with different data.

2. *Bilby Markov chain Monte Carlo Parameter Estimation*

BILBY-MCMC algorithms use a sequential stepping process to generate correlated samples from the target distribution. Specifically, applying the Metropolis-Hastings algorithm facilitates the production of samples from the target density. A random draw from the prior distribution $P(\theta)$ is utilized to initialize the chain, and then the Metropolis-Hastings algorithm is iterated to generate a chain θ_i containing m samples. Typically, these samples in the chain exhibit correlation by selecting a subset of $\frac{m}{\tau}$ samples, where τ is the autocorrelation time (ACT) of the chain. To obtain independent samples, one can select a subset by sampling every τ steps from the chain of samples. The algorithm is being iterated until the stopping criteria are reached. The stopping criteria are given by

$$n_{samples} \geq \frac{m - n_{burn}}{\gamma\tau}, \tag{17}$$

where n_{burn} represents the number of samples discarded to eliminate the chain initialization, while $\gamma \leq 1$ denotes a thinning factor.

H. Likelihood Ratio and GWs Searching

In GWs PE, the likelihood ratio $\mathcal{L}_r$ given by

$$\mathcal{L}_r = \frac{P(\theta \mid s)}{P(\theta \mid n)} = \frac{P(\theta \mid s)}{P(\theta \mid (d - s))}, \tag{18}$$

where s is the signal, d is the data, and $n = d - s$ is the noise. $\mathcal{L}$ is the probability ratio of θ describing the (best-fit) signal to θ describing the residue after subtracting the signal from the data noise. In GWs searching, the match value cannot be used to determine the match between the GWs signal in the data and the template waveform due to noise. Therefore, the likelihood ratio $\mathcal{L}_r$ can be computed by replacing θ with template waveforms t. The likelihood ratio $\mathcal{L}_r$ is denoted by

$$\mathcal{L}_r = \frac{P(t \mid s)}{P(t \mid n)} = \frac{P(t \mid s)}{P(t \mid (d - s))}. \tag{19}$$

The $\mathcal{L}_r$ in searching is the probability ratio of the template waveform describing the signal to the template waveform describing the noise. The larger the $\mathcal{L}_r$, the more likely the signal is present in the data.

I. Rate of Change of Eccentricity

According to a study[26], the time average of the rate of change of eccentricity of the orbit is given by:

$$\left\langle \frac{de}{dt} \right\rangle = -\frac{304eG^3 m_1 m_2 (m_1 + m_2)}{15c^5 a^4 (1 - e^2)^{5/2}} \left(1 + \frac{121e^2}{304}\right). \tag{20}$$

Using this equation, we can evolve the eccentricity of eccentric BBH orbit as it inspirals and approaches merger.

II. OBJECTIVE

The research aims to evaluate the properties of existing and newly-developed GWs waveforms that incorporate the effects of non-zero eccentricity in the binary orbit. The result of eccentricity on GWs waveforms and their detectability in LIGO has been shown in past studies[27],[28]. The existing data will be analyzed to compare eccentric and non-eccentric waveforms, and more detailed studies regarding this parameter will be conducted. This research will also analyze existing data and compare eccentric and non-eccentric waveforms to achieve these goals. This will provide insights into the effects of eccentricity on the waveform, which will then be used to conduct more in-depth studies on this parameter.

During the research period, eccentric waveforms are being studied in the following aspects:

1. Do the eccentric waveforms pass a set of Sanity checks in which they look reasonable and have proper limiting behavior?

2. Comparison between eccentric and non-eccentric waveforms.

3. Is it possible to find the eccentric waveform using a quasi-circular waveform in our template bank?

4. Find out the minimum eccentricity with which the eccentric waveform cannot be distinguished from a regular waveform.

5. By investigating their differences, try to distinguish eccentric waveforms and precessing waveforms.

6. How does the eccentricity evolve with time as the binary system approaches merger?

7. What do eccentric waveforms look like in the time and frequency domain?

8. Develop a framework to calculate the eccentricity value when constructing parameter estimation.

9. How can eccentric waveforms be searched with parameter estimation?

Since current research regarding eccentric gravitational waveforms only considers small eccentricity, studying eccentricity in gravitational waveforms, regardless of its magnitude, is crucial as it can provide a more comprehensive understanding of the behavior of compact binary systems in a broader range of eccentricities. This research can shed light on the physics behind the inspiral and merger of binaries with higher eccentricities, which can lead to the detection of more GWs signals from such systems. Moreover, it can help improve our existing models for the dynamics of compact binaries, which can lead to more accurate parameter estimation and GWs detection. Studying high eccentricities can also help us understand the astrophysical processes responsible for producing such systems and their implications for cosmology and astrophysics. Therefore, this research can have a significant impact on understanding the universe and the properties of compact objects such as neutron stars and black holes.

III. METHODS

To conduct this study, simulated eccentric waveforms with different magnitudes of eccentricity will be generated. To identify apparent differences, these waveforms will be compared to standard quasi-circular waveforms using matched-filtering and sanity checks. The study of eccentric waveforms involves using waveform overlap with standard waveforms. By comparing them, we can quantify the waveforms using parameter estimation, ensuring that eccentricity is considered when generating or detecting GWs signals.

The next step involves performing an injection study to simulate the GWs search process. GWs waveforms with random eccentricity will be injected into random noise. The simulation will search for the waveforms and find out the estimated eccentricity of the signal using Bilby.

The injection study will allow researchers to understand better the properties of eccentric waveforms and how they differ from regular waveforms. This information can then be used to improve the detection of GWs from eccentric sources, such as binary systems with large eccentricities.

After that, more parameters besides eccentricity will be randomized before injecting into random noise. BILBY-MCMC will be used to estimate all the unknown parameters of the injected waveforms. With sufficient testing and correct results, the simulation will be applied to actual data.

I will study eccentric waveforms by the following steps in short:

1. Generate eccentric and non-eccentric waveforms

2. Compare the waveforms

3. Quantify the waveform overlaps

4. Compute and plot the match in both the time and frequency domain

5. Repeat Steps 1 to 4 for similar eccentricity

6. Repeat Steps 1 to 4 for precessing waveforms to determine whether eccentric waveforms can be distinguished from precessing waveforms

7. Construct a 1D simulation that search for the signal with random eccentricity, which is injected into random Gaussian noise

8. Calculate the likelihood between the injected signal and the best-matched template waveform

9. Construct a 2D and 3D simulation similar to Step 7 with two and three unknowns, respectively

10. Construct a search pipeline that can be used for searching eccentric waveforms in real data

11. Construct a PE to estimate the eccentricity and other parameters of GWs events in the simulation

12. Apply the simulation to real data

IV. TIMELINE

During the first half of the research period, the newly-developed waveform, TEOBResumS, was studied and reviewed to check for its precision in simulating zero eccentric GWs waveforms and eccentric GWs waveforms. A TEOBResumS waveform model reviewing Python Jupyter

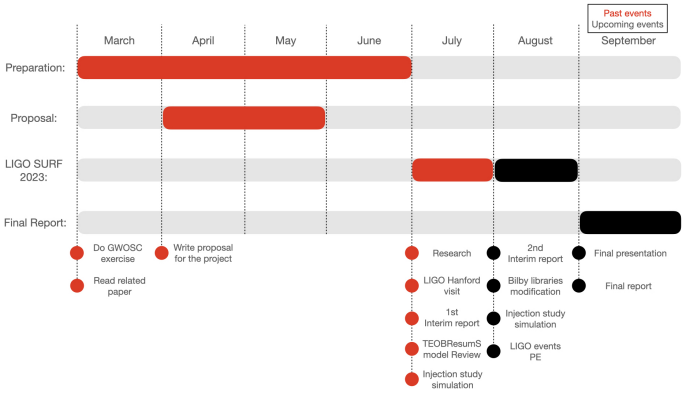

Figure 4. Timeline of the project.

notebook with codes and plots is being written. The notebook works as a preliminary waveform model review.

A simulation is under construction to inject eccentric waveforms into a random Gaussian noise and to search for the waveforms and their eccentricity value by matched filtering and PE using BILBY-MCMC to study detectability. Since the TEOBResumS waveform model is not included in the Bilby libraries, the Bilby libraries are being modified.

In the coming second half of the research period, the accuracy of the TEOBResumS waveform model and the reviewing notebook will be finalized by comparing it with the Simulating eXtreme Spacetimes (SXS) templates[29, 30]. The injection study simulation will be completed with numerous tests. Multi-parameter searching and PE will also be constructed in the simulation. Once the simulation conforms to a sure accuracy, it will be applied to real LIGO GWs data throughout the four observing runs.

V. PROGRESS UPDATE

Eccentric waveforms are the key to this research. Generally, there are three different major GWs models of waveforms, the post-Newtonian template[31], the SXS templates, and the TEOBResumS templates[32, 33]. In the template bank of the post-Newtonian GWs model, eccentric waveforms generated do not contain merger and ringdown. Only templates from SXS and TEOBResumS can be eccentric. TEOBResumS templates are new and are currently not used for data analysis in LIGO. However, eccentric waveforms from SXS are limited. To generate waveforms with variable eccentricities for my search, it is necessary to review the precision of the TEOBResumS templates.

A. Eccentricity Evolution Investigation

According to a study[26], the time average of the rate of change of eccentricity of the orbit is given by:

$$\left\langle \frac{de}{dt} \right\rangle = -\frac{304eG^3m_1m_2(m_1+m_2)}{15c^5a^4(1-e^2)^{5/2}}\left(1+\frac{121e^2}{304}\right). \tag{21}$$

Using this equation, we can evolve the eccentricity of eccentric BBH orbit as it inspirals and approaches merger.

Equation 20 is being reviewed and verified by simulating the merger process between two BH. The simulation shows that the higher the initial eccentricity, the smaller the inspiral time between them, shown in Figure 5. Figure 6 also shows a similar result, with the y-axis being the orbital separation between the two BH. From Figure 7, with a high initial eccentricity of the orbit ($\varepsilon_0 = 0.9$), the orbital separation drops significantly when the $\varepsilon \geq 0.7$ and $\varepsilon \leq 0.1$. The orbital separation drops slowly when the eccentricity of the orbit is at the range $0.1 < \varepsilon < 0.7$. These plots indicate that it is possible to estimate the initial eccentricity ε_0 of the orbit when the eccentricity of the orbit at $f_{GW} = 20Hz$ is measured.

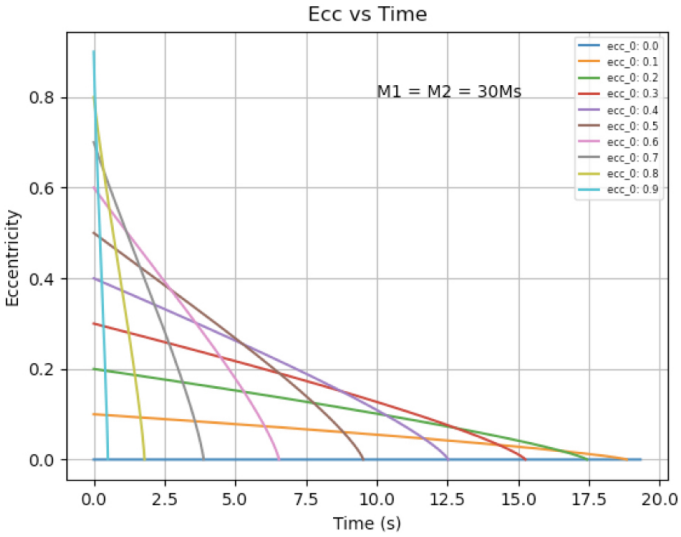

Figure 5. Change of eccentricity of the orbit in time.

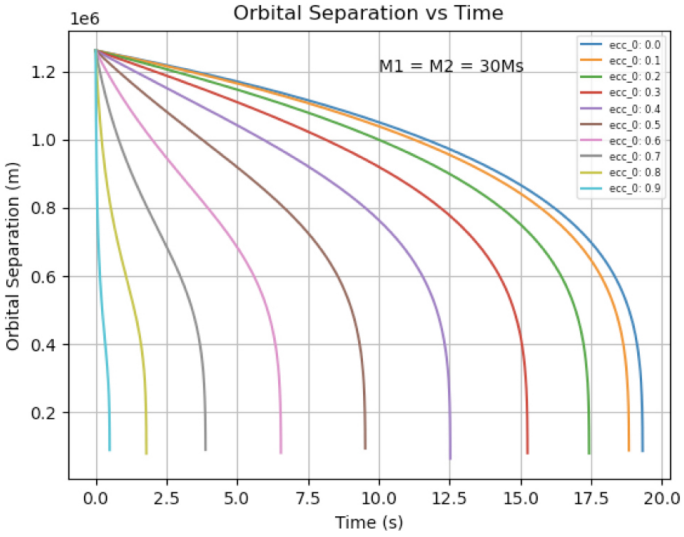

Figure 6. Change of orbital separation in time.

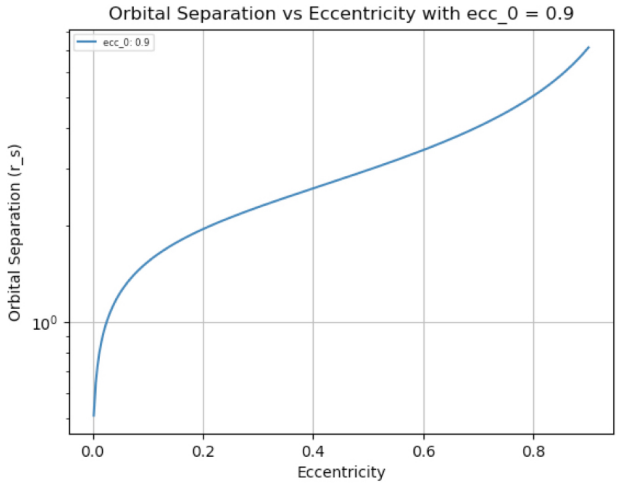

Figure 7. Change of orbital separation in the eccentricity of the orbit.

B. TEOBResumS Waveforms Model Reviewing Notebook

The notebook includes the following tests:

- Individual tests[1]
  - Test for the upper limit of eccentricity in which the waveform can be generated
  - Test for the behavior of the waveform with different eccentricities
  - Test for the total mass of the compact binaries to ensure the waveform varies smoothly
  - Test for the mass ratio of the compact binaries to ensure a smooth waveform can be generated
  - Test for the aligned spin of compact binaries to ensure a smooth waveform can be generated
  - Test for extreme cases of eccentricity, masses, and mass ratio
- Waveform Comparison and Matches[2][3]
  - Comparison between Eccentric TEOBResumS and Non-eccentric TEOBResumS waveforms
  - Comparison between Aligned-spin TEOBResumS and Eccentric TEOB waveforms
  - Comparison between Eccentric TEOBResumS and Eccentric SXS waveforms
  - Comparison between Eccentric TEOBResumS and Eccentric TaylorF2Ecc
  - Comparison between Eccentric TEOBResumS and Eccentric EccentricFD
  - Comparison between align spin TEOBResumS and align spin IMRPhenomXPHM waveforms
  - Comparison between Eccentric TEOBResumS and Precessing IMRPhenomXPHM waveforms

1. *Test for the upper limit of eccentricity in which the waveform can be generated*

Figure 8 shows that a GWs waveform with initial eccentricity $\varepsilon_0 = 0.99982$ at $f_{GW} = 20Hz$ gives a reasonable plot. However, the waveform becomes abnormal when the ε_0 reaches 0.99984, shown in Figure 9. Therefore, we can conclude that the upper limit of eccentricity, which can be inputted, is 0.99982. Waveforms with eccentricity higher than 0.99982 may fail.

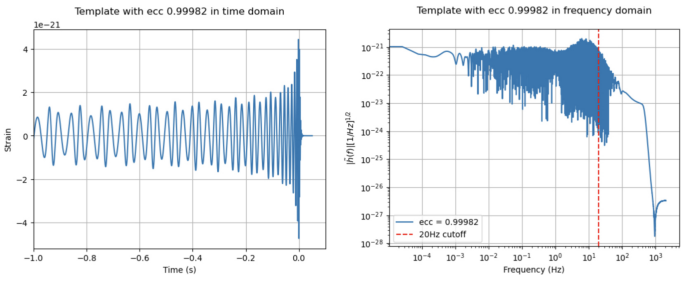

Figure 8. GWs waveform with $\varepsilon_0 = 0.99982$ in the time domain (left) and in the frequency domain (right).

[1] Link to the Reviewing Notebook 1

[2] Link to the Reviewing Notebook 2

[3] Link to the Reviewing Notebook 3

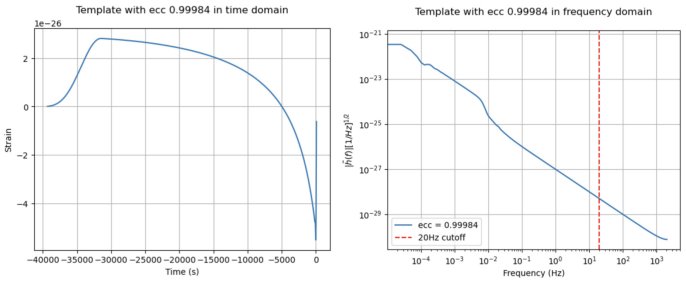

Figure 9. GWs waveform with $\varepsilon_0 = 0.99984$ in the time domain (left) and in the frequency domain (right).

2. *Test for the behavior of the waveform with different eccentricities*

By observing the waveforms with ε_0 from 0.0 to 0.9, the higher the eccentricity of the waveform, the sine wave collapses with more spikes. Figure 10 shows the waveforms in both the time and frequency domain. Waveforms with eccentricity fluctuate before the merger, with vigor depending on the eccentricity. Figure 11 shows how the sine wave collapse when ε_0 is high compared to when ε_0 is low.

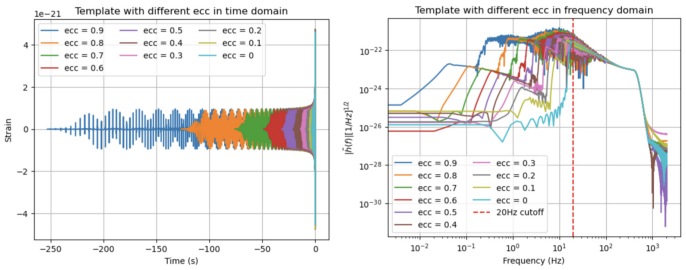

Figure 10. GWs waveform with different ε_0 in the time domain (left) and in the frequency domain (right).

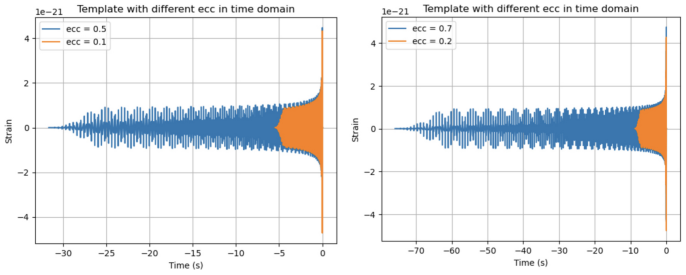

Figure 11. GWs waveform comparison between $\varepsilon_0 = 0.9$ and $\varepsilon_0 = 0.1$ (left) and between $\varepsilon_0 = 0.7$ and $\varepsilon_0 = 0.2$(right).

3. *Test for the total mass of the compact binaries to ensure the waveform varies smoothly*

According to the plots, the waveform behaves reasonably by observing with bare eyes. Figure 12 shows two plots with the waveforms with $\varepsilon_0 = 0.0$ and total mass from $10M_\odot$ to $100M_\odot$ and $110M_\odot$ to $200M_\odot$ in the time domain, while Figure 13 shows in the frequency domain. Figure 14 shows two plots with the waveforms with $\varepsilon_0 = 0.9$ and total mass from $10M_\odot$ to $100M_\odot$ and $110M_\odot$ to $200M_\odot$ in the time domain, while Figure 15 shows in the frequency domain.

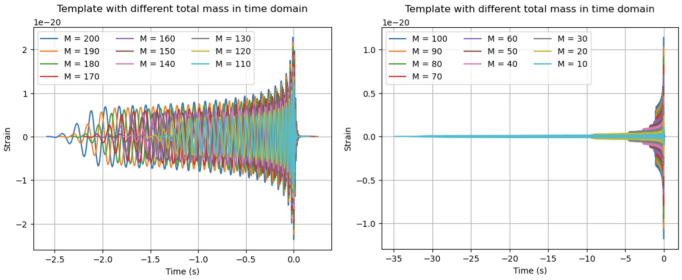

Figure 12. Waveforms in the time domain with $\varepsilon_0 = 0.0$ and total mass from $10M_\odot$ to $100M_\odot$ (left) and from $110M_\odot$ to $200M_\odot$ (right).

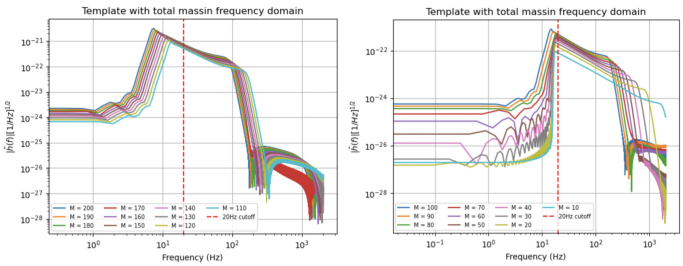

Figure 13. Waveforms in the frequency domain with $\varepsilon_0 = 0.0$ and total mass from $10M_\odot$ to $100M_\odot$ (left) and from $110M_\odot$ to $200M_\odot$ (right).

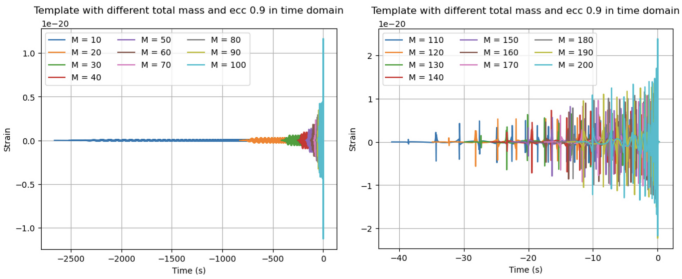

Figure 14. Waveforms in the time domain with $\varepsilon_0 = 0.9$ and total mass from $10M_\odot$ to $100M_\odot$ (left) and from $110M_\odot$ to $200M_\odot$ (right).

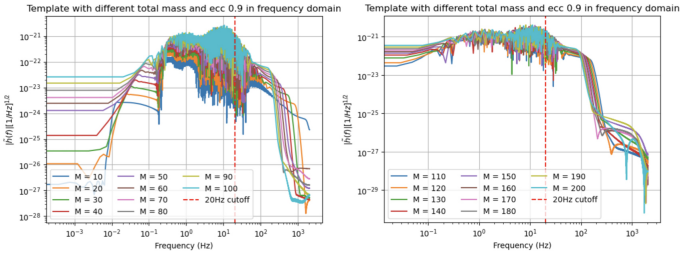

Figure 15. Waveforms in the frequency domain with $\varepsilon_0 = 0.9$ and total mass from $10M_\odot$ to $100M_\odot$ (left) and from $110M_\odot$ to $200M_\odot$ (right).

The larger the total mass, the lower the frequency, right before the binary gets into a merger, which is expected. When the total mass is 800 solar masses, the binary is near the merger state when the GWs frequency is at 20Hz, which the complete waveform can hardly be detected with our current detectors. Figure 16 and Figure 17 show how the waveform when the total mass reaches the upper limit with $\varepsilon_0 = 0.0$ and $\varepsilon_0 = 0.9$, respectively. Therefore, we can conclude that the upper limit of the total mass is $800M_\odot$.

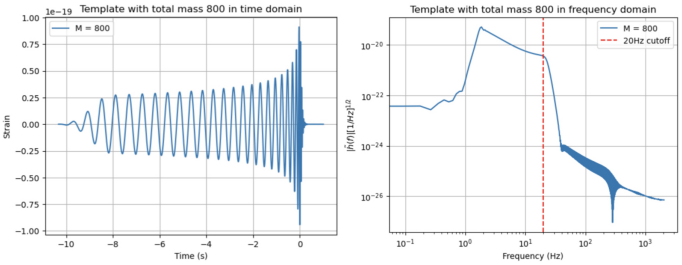

Figure 16. Waveforms with $\varepsilon_0 = 0.0$ and total mass $800M_\odot$ in the time domain (left) and in the frequency domain (right).

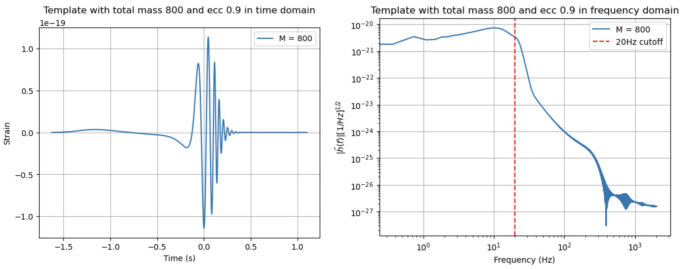

Figure 17. Waveforms with $\varepsilon_0 = 0.9$ and total mass $800M_\odot$ in the time domain (left) and in the frequency domain (right).

4. Test for the mass ratio of the compact binaries to ensure a smooth waveform can be generated

According to the plots, the waveform behaves reasonably by observing with bare eyes. Figure 18 shows two plots with the waveforms with $\varepsilon_0 = 0.0$ and mass ratio from 1 to 7 and 8 to 14 in the time domain, while Figure 19 shows in the frequency domain. Figure 20 shows two plots with the waveforms with $\varepsilon_0 = 0.9$ and mass ratio from 1 to 7 and 8 to 14 in the time domain, while Figure 21 shows in the frequency domain.

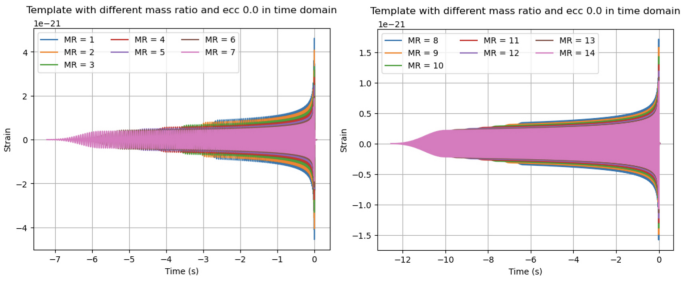

Figure 18. Waveforms in the time domain with $\varepsilon_0 = 0.0$ and mass ratio from 1 to 7 (left) and from 8 to 14 (right).

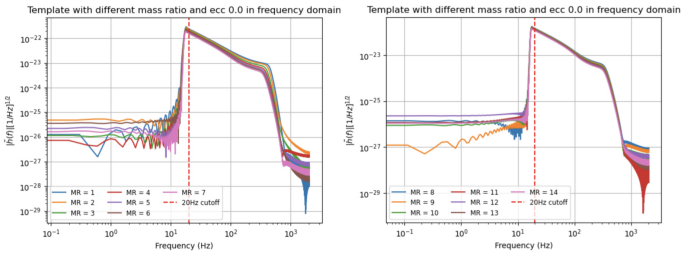

Figure 19. Waveforms in the frequency domain with $\varepsilon_0 = 0.0$ and mass ratio from 1 to 7 (left) and from 8 to 14 (right).

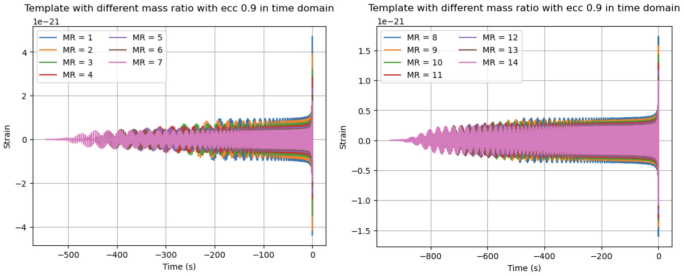

Figure 20. Waveforms in the time domain with $\varepsilon_0 = 0.9$ and mass ratio from 1 to 7 (left) and from 8 to 14 (right).

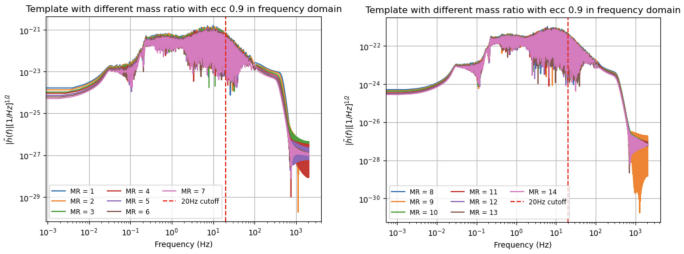

Figure 21. Waveforms in the time domain with $\varepsilon_0 = 0.9$ and mass ratio from 1 to 7 (left) and from 8 to 14 (right).

The plots also show that the waveform observes typically with bare eyes. With no eccentricity, the mass ratio can be set to 10000. However, if the eccentricity of the waveform is 0.9, the waveform fails with a mass ratio of 1000. Figure 22 shows the waveform with $\varepsilon_0 = 0.0$ and mass ratio 1000, while Figure 23 shows that with $\varepsilon_0 = 0.9$ and mass ratio 100.

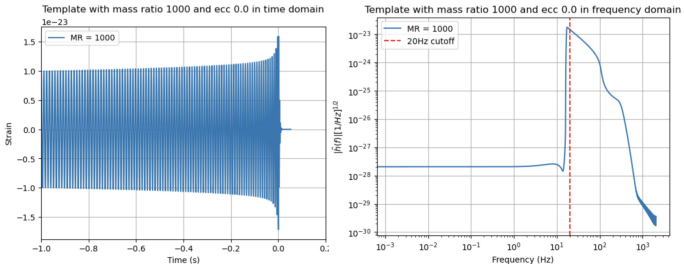

Figure 22. Waveforms with $\varepsilon_0 = 0.0$ and mass ratio 1000 in the time domain (left) and in the frequency domain (right).

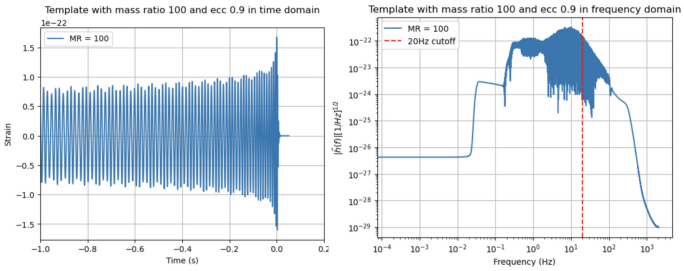

Figure 23. Waveforms with $\varepsilon_0 = 0.9$ and mass ratio 1000 in the time domain (left) and in the frequency domain (right).

5. Test for the aligned spin of compact binaries to ensure a smooth waveform can be generated

According to the plots, TEOBResumS can generate aligned spin waveforms up to 1.0. Figure 24 shows two plots with the waveforms with $\varepsilon_0 = 0.0$ and spin from 0.0 to 0.5 and 0.6 to 1.0 in the time domain, while Figure 25 shows in the frequency domain. Figure 26 shows two plots with the waveforms with $\varepsilon_0 = 0.9$ and spin from 0.0 to 0.5 and 0.6 to 1.0 in the time domain, while Figure 27 shows in the frequency domain. From the plots, the waveforms vary smoothly and in a reasonable way. This proves the compatibility of TEOBResumS to aligned-spin waveform generating.

6. Test for extreme cases for eccentricity, masses, mass ratio, and aligned spin

The extreme cases for maximizing the eccentricity, masses, mass ratio, and aligned spin are tested. By testing, the maximum combination is $\varepsilon_0 = 0.999$, total mass = 450$M_\odot$, mass ratio = 45, and aligned spin = 1.0, as shown in Figure 28. Parameters higher than these values may lead to the failure of the waveform.

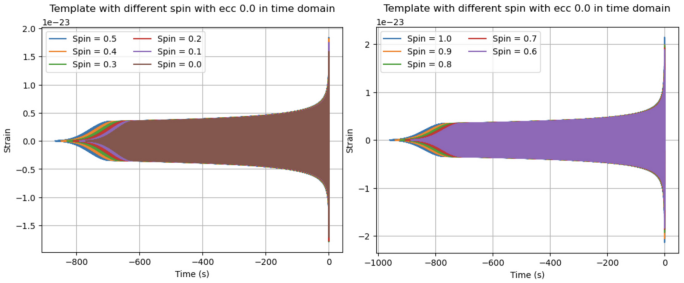

Figure 24. Waveforms in the time domain with $\varepsilon_0 = 0.0$ and aligned-spin from 0.0 to 0.5 (left) and from 0.6 to 1.0 (right).

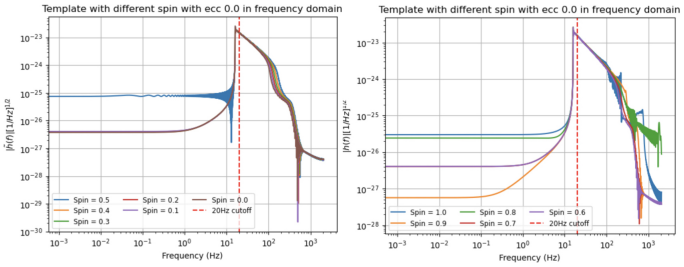

Figure 25. Waveforms in the frequency domain with $\varepsilon_0 = 0.0$ aligned-spin from 0.0 to 0.5 (left) and from 0.6 to 1.0 (right).

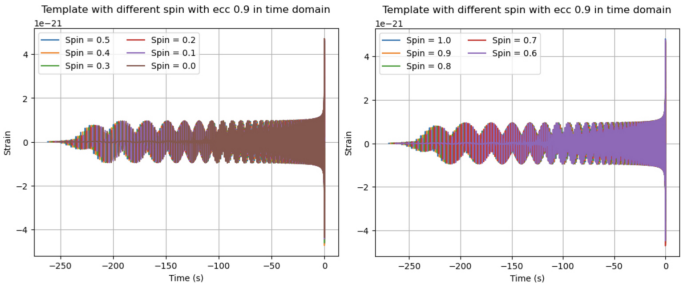

Figure 26. Waveforms in the time domain with $\varepsilon_0 = 0.9$ and aligned-spin from 0.0 to 0.5 (left) and from 0.6 to 1.0 (right).

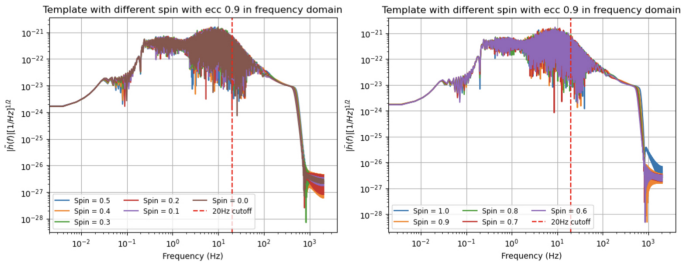

Figure 27. Waveforms in the frequency domain with $\varepsilon_0 = 0.9$ aligned-spin from 0.0 to 0.5 (left) and from 0.6 to 1.0 (right).

C. Waveform Comparison and Matches

A simple matching model is being constructed to do waveform overlapping and match calculating between pairs of eccentric waveforms and non-eccentric waveforms and pairs of eccentric waveforms and precessing waveforms in both the

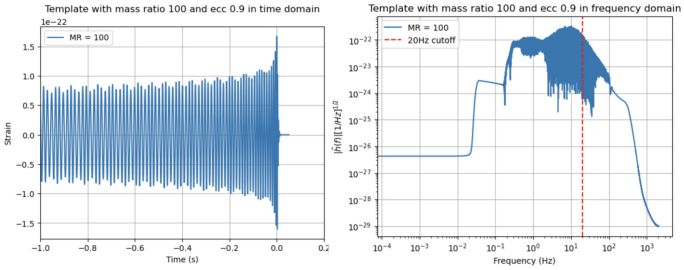

Figure 28. Waveforms with $\varepsilon_0 = 0.999$, mass ratio 100 and total mass $450M_\odot$ in the time domain (left) and in the frequency domain (right).

time domain and frequency domain. The simulation uses waveforms with different eccentricities to overlap and calculate the match. After calculating the matches, graphs of the match against the eccentricity of the testing waveform are plotted.

1. *Comparison between Eccentric TEOBResumS and Non-eccentric TEOBResumS waveforms*

Figure 29 shows the waveforms of eccentric TEOBResumS with different ε_0 and non-eccentric TEOBResumS waveforms. Figure 30 and 31 shows the waveforms of eccentric TEOBResumS with $\varepsilon_0 = 0$ and non-eccentric TEOBResumS waveforms with mass ratio 1 and 15, respectively. The plots show that the eccentric TEOB waveform with $\varepsilon_0 = 0$ is precisely the same (match values are 1 in both time domain and frequency domain) as the non-eccentric TEOB waveform with mass ratios 1 and 15. This proves the compatibility between eccentric TEOB and non-eccentric TEOB waveforms.

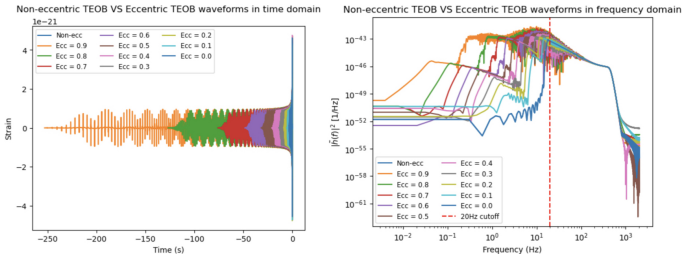

Figure 29. Eccentric TEOBResumS with different eccentricity and Non-eccentric TEOBResumS waveforms in the time domain (left) and frequency domain (right).

2. *Comparison between Aligned-spin TEOBResumS and Eccentric TEOB waveforms*

Figure 32 shows the waveforms of eccentric TEOBResumS with $\varepsilon_0 = 0.2$, and spin 1 and spin2 equal 0.2 in both the time and frequency domain. Figure 33 shows the waveforms of eccentric TEOBResumS with $\varepsilon_0 = 0.6$, and spin 1 and spin2 equal 0.6 in both the time and frequency domain. Figure 34 shows the waveforms of eccentric TEOBResumS with $\varepsilon_0 = 0.8$, and spin 1 and spin2 equal 1.0 in both the time and frequency domain. According to the plots, once the spin is added to the waveform, it differs from an eccentric waveform with a low match value between them. This proves that an aligned-spin waveform is distinguishable from an eccentric waveform.

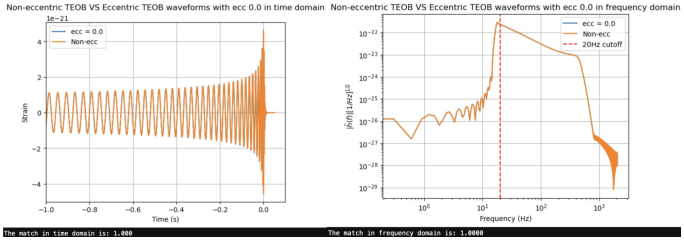

Figure 30. Eccentric TEOBResumS with $\varepsilon_0 = 0$ and Non-eccentric TEOBResumS waveforms with mass ratio 1 in the time domain (left) and frequency domain (right) with match value.

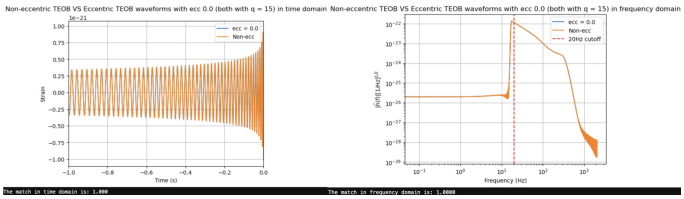

Figure 31. Eccentric TEOBResumS with $\varepsilon_0 = 0$ and Non-eccentric TEOBResumS waveforms with mass ratio 15 in the time domain (left) and frequency domain (right) with match value.

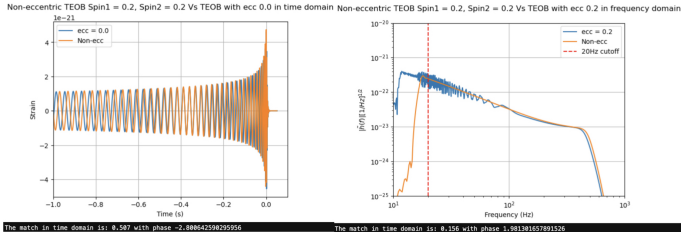

Figure 32. Eccentric TEOBResumS with $\varepsilon_0 = 0.2$ and aligned-spin TEOBResumS waveforms with spin 1 = 0.2 and spin 2 = 0.2 in the time domain (left) and frequency domain (right).

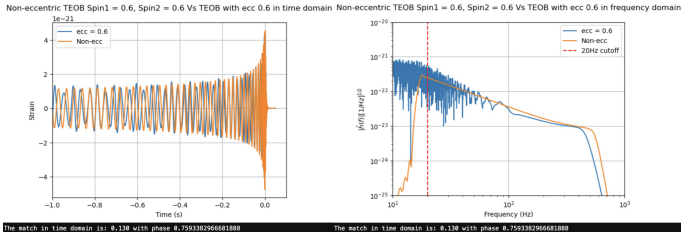

Figure 33. Eccentric TEOBResumS with $\varepsilon_0 = 0.6$ and aligned-spin TEOBResumS waveforms with spin 1 = 0.6 and spin 2 = 0.6 in the time domain (left) and frequency domain (right).

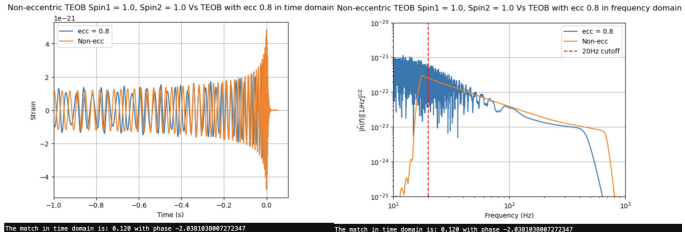

Figure 34. Eccentric TEOBResumS with $\varepsilon_0 = 0.8$ and aligned-spin TEOBResumS waveforms with spin 1 = 1.0 and spin 2 = 1.0 in the time domain (left) and frequency domain (right).

3. *Comparison between Eccentric TEOBResumS and SXS waveforms*

From the plots and calculated match values, most of the waveforms generated using TEOBResumS are highly similar to that from the SXS catalog (match value ¿= 0.85 in both time and frequency domains). This proves the reliability of TEOBResumS waveforms with variable eccentricity values. Figure 35 compares BBH 1569 from the SXS catalog with $\varepsilon_0 = 1.341x10^{-4}$ which is neglectable, and TEOB waveform with the same parameters as SXS in both the time and frequency domains. Figure 36 compares BBH 1373 from the SXS catalog with $\varepsilon_0 = 0.2087$ and TEOB waveform with the same parameters as SXS in both the time and frequency domains. Figure 37 compares BBH 1360 from the SXS catalog with $\varepsilon_0 = 0.3636$ and TEOB waveform with the same parameters as SXS in both the time and frequency domains.

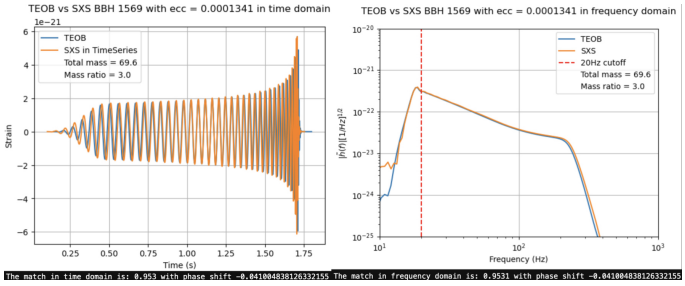

Figure 35. BBH 1569 from SXS and TEOBResumS waveforms with $\varepsilon_0 = 1.341 * 10^{-4}$ in the time domain (left) and frequency domain (right).

4. *Comparison between Eccentric TEOBResumS and Eccentric TaylorF2Ecc*

From the plots, the TaylorF2Ecc waveforms have waveform modulations even when the eccentricity is zero, as shown in Figure 38. Waveforms of it also have unreasonable fluctuations at other eccentricities compared to TEOBResumS. According to the plots, TEOBResumS waveforms are much more reliable than TaylorF2Ecc waveforms calculated from the Post-Newtonian method.

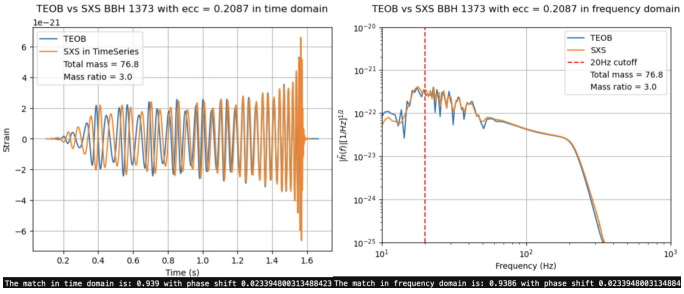

Figure 36. BBH 1373 from SXS and TEOBResumS waveforms with $\varepsilon_0 = 0.2087$ in the time domain (left) and frequency domain (right).

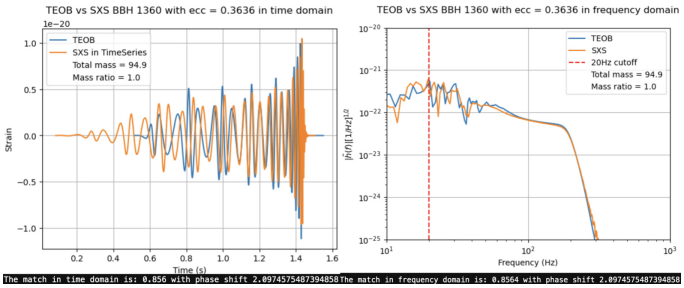

Figure 37. BBH 1360 from SXS and TEOBResumS waveforms with $\varepsilon_0 = 0.3636$ in the time domain (left) and frequency domain (right).

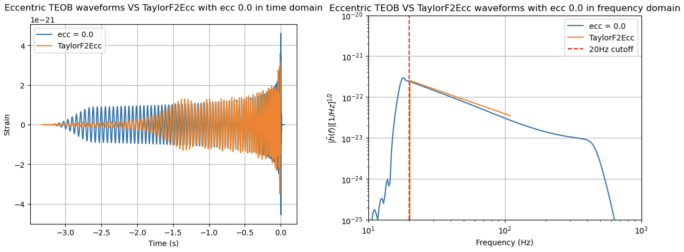

Figure 38. TaylorF2Ecc and TEOBResumS waveforms with $\varepsilon_0 = 0$ in the time domain (left) and frequency domain (right).

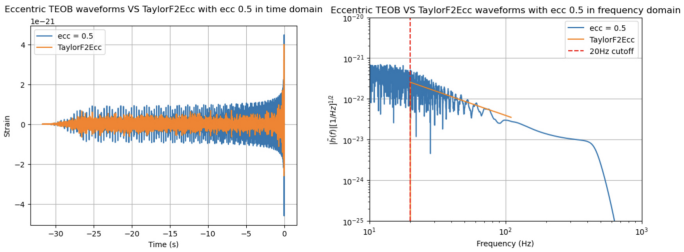

Figure 39. TaylorF2Ecc and TEOBResumS waveforms with $\varepsilon_0 = 0.5$ in the time domain (left) and frequency domain (right).

5. *Comparison between Eccentric TEOBResumS and Eccentric EccentricFD*

From the plots, the EccentricFD waveforms have waveform modulations even when the eccentricity is zero, as shown in Figure 41. Waveforms of it also have unreasonable fluctuations at other eccentricities compared to TEOBResumS.

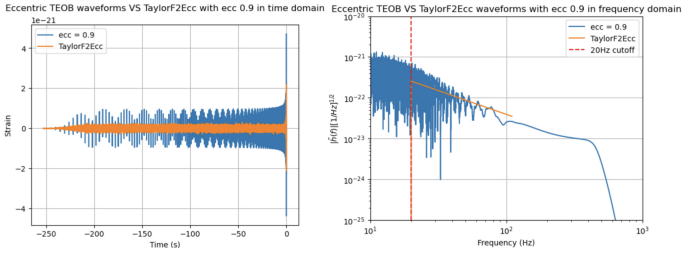

Figure 40. TaylorF2Ecc and TEOBResumS waveforms with $\varepsilon_0 = 0.9$ in the time domain (left) and frequency domain (right).

The result of this section and the previous section shows that a more accurate eccentric waveform model is needed. Therefore from the plots, TEOBResumS waveforms are much more reliable than EccentricFD waveforms calculated from the Post-Newtonian method.

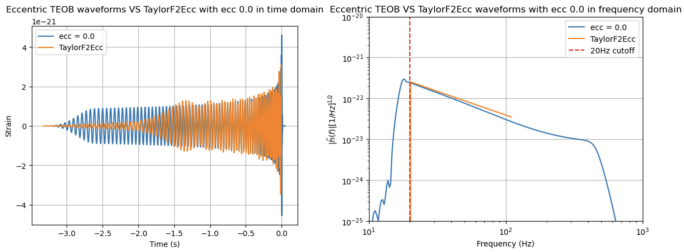

Figure 41. EccentricFD and TEOBResumS waveforms with $\varepsilon_0 = 0$ in the time domain (left) and frequency domain (right).

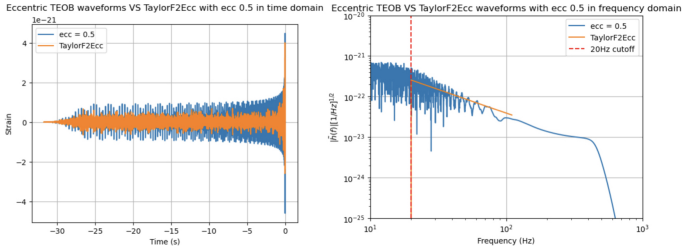

Figure 42. EccentricFD and TEOBResumS waveforms with $\varepsilon_0 = 0.5$ in the time domain (left) and frequency domain (right).

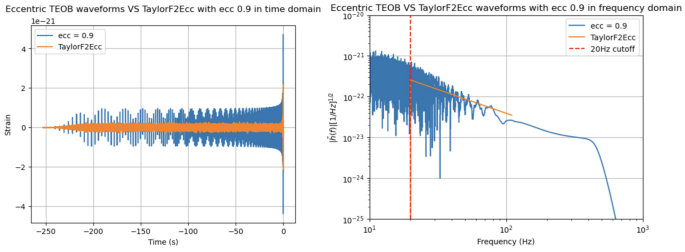

Figure 43. EccentricFD and TEOBResumS waveforms with $\varepsilon_0 = 0.9$ in the time domain (left) and frequency domain (right).

6. *Comparison between align spin TEOBResumS and align spin IMRPhenomXPHM waveforms*

From the plots, the aligned spin waveforms generated with TEOBResumS are nearly the same as that with IMRPhenonXPHM. Figure 44 to Figure 46 shows aligned-spin TEOB and aligned-spin IMRPhenomXPHM on the same graph with different values of aligned-spin in the time and frequency domains. This proves that the calculations in the aligned spin of the TEOBResumS waveform generator are accurate.

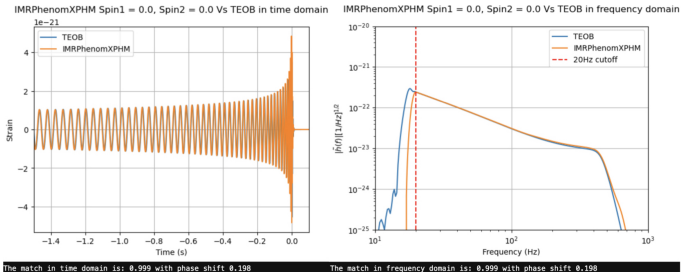

Figure 44. IMRPhenomXPHM and TEOBResumS waveforms with spin 1 and spin 2 equal 0.0 in the time domain (left) and frequency domain (right).

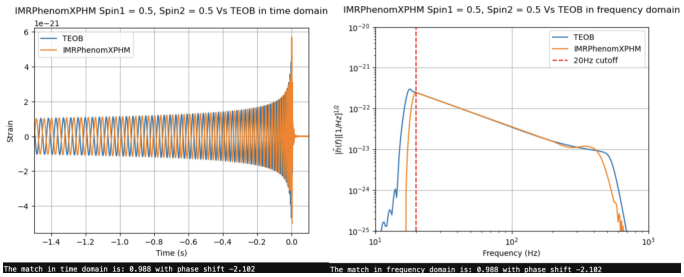

Figure 45. IMRPhenomXPHM and TEOBResumS waveforms with spin 1 and spin 2 equal 0.5 in the time domain (left) and frequency domain (right).

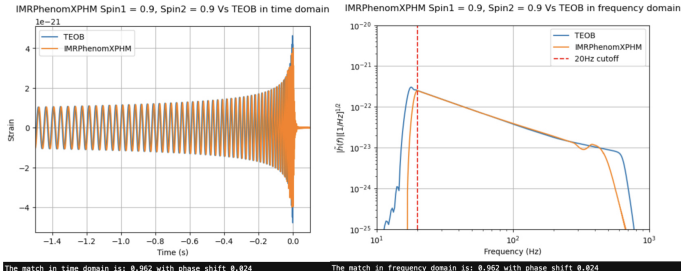

Figure 46. IMRPhenomXPHM and TEOBResumS waveforms with spin 1 and spin 2 equal 0.9 in the time domain (left) and frequency domain (right).

7. *Comparison between Eccentric TEOBResumS and Precessing IMRPhenomXPHM waveforms*

Observing the plots in the time domain shows that the amplitude modulation of precessing waveforms processes smoothly, while the amplitude of eccentric waveforms fluctuates vigorously before the merger. It would be hard to distinguish between precessing and non-precessing waveforms with zero eccentricity, as shown in Figure 47 and Figure 50. However, when eccentricity involves, the match value between precessing waveform and eccentric waveform will be lower than that of precessing waveform and non-precessing waveform with zero eccentricity. The higher the eccentricity, the lower the match between the precessing waveform and the non-precessing waveform with zero eccentricity. This acts as an evidence that waveforms can be able to distinguish from precessing waveforms.

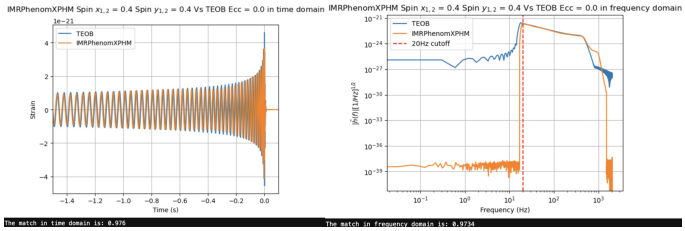

Figure 47. Eccentric TEOBResumS with $\varepsilon_0 = 0.0$ and precessing IMRPhenonXPHM waveforms with $S_x = 0.4$ and $S_y = 0.4$ in the time domain (left) and frequency domain (right).

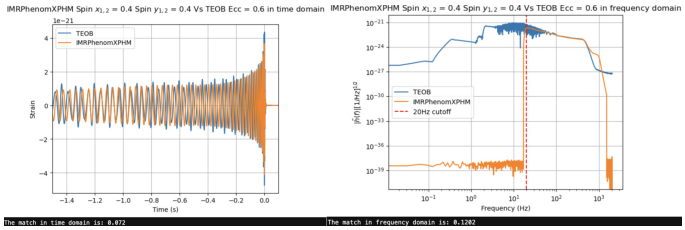

Figure 48. Eccentric TEOBResumS with $\varepsilon_0 = 0.6$ and precessing IMRPhenonXPHM waveforms with $S_x = 0.4$ and $S_y = 0.4$ in the time domain (left) and frequency domain (right).

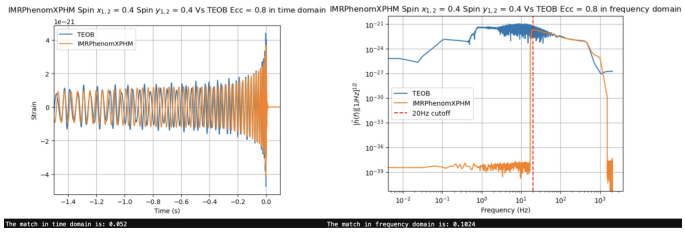

Figure 49. Eccentric TEOBResumS with $\varepsilon_0 = 0.8$ and precessing IMRPhenonXPHM waveforms with $S_x = 0.4$ and $S_y = 0.4$ in the time domain (left) and frequency domain (right).

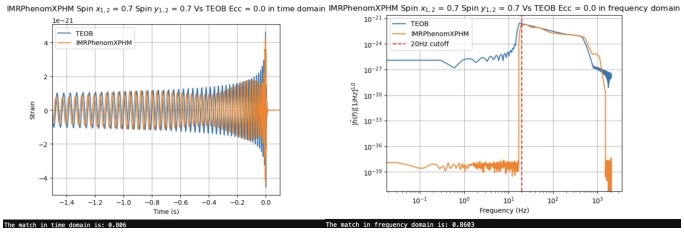

Figure 50. Eccentric TEOBResumS with $\varepsilon_0 = 0.0$ and precessing IMRPhenonXPHM waveforms with $S_x = 0.7$ and $S_y = 0.7$ in the time domain (left) and frequency domain (right).

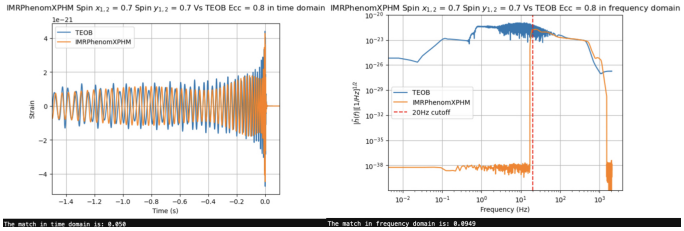

Figure 51. Eccentric TEOBResumS with $\varepsilon_0 = 0.8$ and precessing IMRPhenonXPHM waveforms with $S_x = 0.7$ and $S_y = 0.7$ in the time domain (left) and frequency domain (right).

D. Future Plan

1. *Eccentric Search Model*

ECcentric searcH mOdel (ECHO) is a search model that uses Bilby to generate TEOBResumS waveforms. This model search for the signal waveform with eccentricity in random Gaussian noise. It then uses Bilby to do PE to map out the possible range of the eccentricity of the signal. If the range of the eccentricity calculated is within a reasonable range, a multi-parameter (total mass of the binary and the mass ratio) PE will be constructed. The model is estimated to be finished by 12^{th} August.

2. *Advanced Eccentric Search Model*

Advanced ECcentric searcH mOdel (aECHO) is a search model similar to ECHO, but real data is used. This model aims to search for eccentric GWs from the LIGO event catalogs from O1 to O3 and the events detected in O4. This model is estimated to be finished by 20^{th} August.

VI. REFERENCES

[1] Indrajit Chakrabarty, "Gravitational waves: An introduction," (1999), arXiv:physics/9908041 [physics.ed-ph].

[2] Maurizio Spurio, "An introduction to astrophysical observables in gravitational wave detections," (2019), arXiv:1906.03643 [astro-ph.HE].

[3] Jan W. van Holten, "Curvature Dynamics in General Relativity," Universe **9**, 110 (2023), arXiv:2211.10123 [gr-qc].

[4] M. Le Delliou, "Advanced General Relativity Notes," (2022) arXiv:2208.02506 [gr-qc].

[5] J. F. Pommaret, "General Relativity and Gauge Theory: Beyond the Mirror," arXiv e-prints , arXiv:2302.06585 (2023), arXiv:2302.06585 [math.GM].

[6] Gary Nash, "Modified General Relativity and dark matter," (2023), 10.1142/S0218271823500311, arXiv:2304.09671 [gr-qc].

[7] Maximiliano Isi, "Parametrizing gravitational-wave polarizations," (2022), arXiv:2208.03372 [gr-qc].

[8] R. Abbott *et al.* (KAGRA, VIRGO, LIGO Scientific), "Population of Merging Compact Binaries Inferred Using Gravitational Waves through GWTC-3," Phys. Rev. X **13**, 011048 (2023), arXiv:2111.03634 [astro-ph.HE].

[9] J. Aasi *et al.* (LIGO Scientific), "Advanced LIGO," Class. Quant. Grav. **32**, 074001 (2015), arXiv:1411.4547 [gr-qc].

[10] F. Acernese *et al.* (VIRGO), "Advanced Virgo: a second-generation interferometric gravitational wave detector," Class. Quant. Grav. **32**, 024001 (2015), arXiv:1408.3978 [gr-qc].

[11] Kentaro Somiya (KAGRA), "Detector configuration of KAGRA: The Japanese cryogenic gravitational-wave detector," Class. Quant. Grav. **29**, 124007 (2012), arXiv:1111.7185 [gr-qc].

[12] B. P. Abbott *et al.* (LIGO Scientific, Virgo), "GWTC-1: A Gravitational-Wave Transient Catalog of Compact Binary Mergers Observed by LIGO and Virgo during the First and Second Observing Runs," Phys. Rev. X **9**, 031040 (2019), arXiv:1811.12907 [astro-ph.HE].

[13] R. Abbott *et al.* (LIGO Scientific, Virgo), "GWTC-2: Compact Binary Coalescences Observed by LIGO and Virgo During the First Half of the Third Observing Run," Phys. Rev. X **11**, 021053 (2021), arXiv:2010.14527 [gr-qc].

[14] R. Abbott *et al.* (LIGO Scientific, VIRGO, KAGRA), "GWTC-3: Compact Binary Coalescences Observed by LIGO and Virgo During the Second Part of the Third Observing Run," (2021), arXiv:2111.03606 [gr-qc].

[15] B. P. Abbott *et al.* (LIGO Scientific, Virgo), "Search for Eccentric Binary Black Hole Mergers with Advanced LIGO and Advanced Virgo during their First and Second Observing Runs," Astrophys. J. **883**, 149 (2019), arXiv:1907.09384 [astro-ph.HE].

[16] Tao Yang, Rong-Gen Cai, Zhoujian Cao, and Hyung Mok Lee, "Parameter estimation of eccentric gravitational waves with a decihertz observatory and its cosmological implications," Phys. Rev. D **107**, 043539 (2023), arXiv:2212.11131 [gr-qc].

[17] Stefano Schmidt, Bhooshan Gadre, and Sarah Caudill, "Gravitational-wave template banks for novel compact binaries," (2023), arXiv:2302.00436 [gr-qc].

[18] Michela Mapelli, "Binary Black Hole Mergers: Formation and Populations," Front. Astron. Space Sci. **7**, 38 (2020), arXiv:2105.12455 [astro-ph.HE].

[19] Bruce Allen, Warren G. Anderson, Patrick R. Brady, Duncan A. Brown, and Jolien D. E. Creighton, "FINDCHIRP: An Algorithm for detection of gravitational waves from inspiraling compact binaries," Phys. Rev. D **85**, 122006 (2012), arXiv:gr-qc/0509116.

[20] Koustav Chandra, V. Villa-Ortega, T. Dent, C. McIsaac, Archana Pai, I. W. Harry, G. S. Cabourn Davies, and K. Soni, "An optimized PyCBC search for gravitational waves from intermediate-mass black hole mergers," Phys. Rev. D **104**, 042004 (2021), arXiv:2106.00193 [gr-qc].

[21] Samantha A. Usman *et al.*, "The PyCBC search for gravitational waves from compact binary coalescence," Class. Quant. Grav. **33**, 215004 (2016), arXiv:1508.02357 [gr-qc].

[22] Derek Davis, Max Trevor, Simone Mozzon, and Laura K. Nuttall, "Incorporating information from LIGO data quality streams into the PyCBC search for gravitational waves," Phys. Rev. D **106**, 102006 (2022), arXiv:2204.03091 [gr-qc].

[23] Gregory Ashton *et al.*, "BILBY: A user-friendly Bayesian inference library for gravitational-wave astronomy," Astrophys. J. Suppl. **241**, 27 (2019), arXiv:1811.02042 [astro-ph.IM].

[24] Nelson Christensen and Renate Meyer, "Parameter estimation with gravitational waves," Rev. Mod. Phys. **94**, 025001 (2022), arXiv:2204.04449 [gr-qc].

[25] Gregory Ashton and Colm Talbot, "B ilby-MCMC: an MCMC sampler for gravitational-wave inference," Mon. Not. Roy. Astron. Soc. **507**, 2037–2051 (2021), arXiv:2106.08730 [gr-qc].

[26] P. C. Peters, "Gravitational radiation and the motion of two point masses," Phys. Rev. **136**, B1224–B1232 (1964).

[27] E. A. Huerta, Prayush Kumar, Sean T. McWilliams, Richard O'Shaughnessy, and Nicolás Yunes, "Accurate and efficient waveforms for compact binaries on eccentric orbits," Phys. Rev. D **90**, 084016 (2014), arXiv:1408.3406 [gr-qc].

[28] Sashwat Tanay, Maria Haney, and Achamveedu Gopakumar, "Frequency and time domain inspiral templates for comparable mass compact binaries in eccentric orbits," Phys. Rev. D **93**, 064031 (2016), arXiv:1602.03081 [gr-qc].

[29] Michael Boyle *et al.*, "The SXS Collaboration catalog of binary black hole simulations," Class. Quant. Grav. **36**, 195006 (2019), arXiv:1904.04831 [gr-qc].

[30] Abdul H. Mroue *et al.*, "Catalog of 174 Binary Black Hole Simulations for Gravitational Wave Astronomy," Phys. Rev. Lett. **111**, 241104 (2013), arXiv:1304.6077 [gr-qc].

[31] Soichiro Isoyama, Riccardo Sturani, and Hiroyuki Nakano, "Post-Newtonian templates for gravitational waves from compact binary inspirals," (2020), 10.1007/978-981-15-4702-$7_3$1 − 1, arXiv:2012.01350 [gr-qc].

[32] Danilo Chiaramello and Alessandro Nagar, "Faithful analytical effective-one-body waveform model for spin-aligned, moderately eccentric, coalescing black hole binaries," Phys. Rev. D **101**, 101501 (2020), arXiv:2001.11736 [gr-qc].

[33] Abhishek V. Joshi, Shawn G. Rosofsky, Roland Haas, and E. A. Huerta, "Numerical relativity higher order gravitational waveforms of eccentric, spinning, nonprecessing binary black hole mergers," Phys. Rev. D **107**, 064038 (2023), arXiv:2210.01852 [gr-qc].